

3D printed multi-functional Ti6Al4V based hybrid scaffold for the management of osteosarcoma

Bianyun Cai^{ab1}, Leizhen Huang^{a1}, Jingcheng Wang^{a1}, Dan Sun^c, Ce Zhu^a, Yong Huang^a, Shujun Li^d,
Zhijun Guo^e, Limin Liu^a, Ganjun Feng^{a*}, Yubao Li^{a*}, Li Zhang^{a*}

^a Analytical & Testing Center, Department of Orthopedic Surgery and Orthopedic Research Institute, West China Hospital, Sichuan University, Chengdu 610065, China

^b College of Medical Technology and Engineering, Henan University of Science and Technology, 263 Kaiyuan Avenue, Luoyang 471023, China

^c Advanced Composite Research Group (ACRG), School of Mechanical and Aerospace Engineering, Queens University Belfast, Belfast BT9 5AH, U.K.

^d Institute of Metal Research, Chinese Academy of Sciences, 72 Wenhua Road, Shenyang 110016, China

^e School of Materials Science and Physics, China University of Mining and Technology, Xuzhou 221116, China

Abstract

Osteosarcoma is a challenging bone disease which is commonly associated with critical sized bone defect and cancer recurrence. Here we designed and developed a multi-functional, hierarchical structured bone scaffold which can meet the demanding requirements for osteosarcoma management. This is the first 3D printed Ti6Al4V scaffold with hydrothermally induced TiO₂/TiP coating offering its unique photothermal conversion property for bone cancer ablation. The scaffold is also infused with drug laden gelatin/hydroxyapatite nanocomposite, which provides the ideal porous structure for cell adhesion / bone ingrowth and promotes bone regeneration. The scaffold has been thoroughly characterized by SEM/EDX, TEM, XPS, XRD, TGA and UV-vis, and its *in vitro* bone cancer ablation efficiency has been validated using MG-63 cells. The hybrid scaffold showed excellent biocompatibility and its osteointegration function has been demonstrated using an animal model.

Highlight

- The first Ti6Al4V based bone scaffold with hierarchical microstructure and multi-functions targeting osteosarcoma management and bone defect repair.
- The first time TiO₂/TiP coating has been deployed for photothermal cancer ablation.
- The infused gelatin/hydroxyapatite nanocomposite provides favorable drug release and bone regeneration property which has been validated *in vitro* and *in vivo*.

Keywords: 3D printing; Ti scaffold; drug release; photothermal; osseointegration; bone regeneration

1. Introduction

Osteosarcoma is the most common primary malignant tumor of the bone, frequently presenting in young people between the ages of 10~14 years and in adults over 65 years. ^[1] The routine treatment protocol for osteosarcoma involves a combination of surgery, radiotherapy and chemotherapy. ^[2] However, the invasive surgery often results in large bone defects beyond the bone's natural ability to self-heal (“critical sized bone defects”), and the tumor recurrences rate is as high as 30~40% in non-metastatic patients. ^[3] Unfortunately, this challenge remained unresolved over the last 40 years, ^[4] which presents an urgent demand for novel and more effective therapeutic strategies.

For repair of critical sized bone defects, implantation of autografts (taken from host) remains the gold standard. However, the procedure is limited by donor site morbidity, postoperative pain, risk of infection and the lack of available tissue. ^[5] Use of allogeneic bone grafts (taken from other donors) is also restricted due to limited/unpredictable bone quality, potential microbiological contamination and immune rejection issue. ^[6] While a large proportion of the osteosarcoma patients urgently require implants to repair their critical sized bone defects, it is hard to meet this demand due to a shortage of suitable surgical implants. This, in addition to the increasing need for structural repair of bone defects due to accidents and other bone related diseases (such as osteoporosis), has driven the research and development in advanced bone repair materials in the past decades.

Three-dimensional (3D) printed bone scaffolds can provide customized implant geometry that meets the stringent requirements of patient’s physiological anatomy in clinical settings. Their pore size/porosity can also be tailored to promote the bone ingrowth, hence accelerating the functional recovery of the defective bone. However, 3D printed ceramic scaffolds (such as calcium phosphate, ^[8] β -TCP, ^[9] Fe-doped akermanite (Fe-AKT), ^[10] etc), suffer from low fracture toughness; whereas 3D printed polymer-based scaffolds (such as PCL, ^[11] PLA, ^[12] PLLA, ^[13] hydrogels, ^[14] etc) do not offer sufficient stiffness and strength, which limit their applications in load bearing bone implants.

Titanium (Ti) and its alloys are commonly utilized for orthopedic and dental implants owing to their excellent mechanical properties, chemical resistance and biocompatibility. ^[15] However, the “stress shielding” resulting from the much higher elastic modulus of Ti (~110 GPa vs 0.3~17 GPa of natural bone) can lead to implant loosening. ^[16] 3D printed Ti alloy scaffolds have attracted considerable interest in orthopaedic applications in recent decades, because its mechanical properties

(such as stiffness) can be tailored to avoid “stress shielding”.^[17] Recent studies show that 3D printed Ti scaffold with a pore size ranging from 350 to 1500 μm can achieve stiffness similar to that of the human bone,^[18, 19] although such pore size is not ideal for cells adherence and migration.^[20]

On the other hand, the lack of initial osseointegration of Ti implant due to its bioinertness also remains a long-standing issue.^[21] Researchers have explored various approaches to modify the Ti alloy composition^[22] and/or Ti surface structure/chemistry.^[23] In a recent study,^[21] our group has developed micro/nanoscaled hierarchical TiO_2/TiP hybrid coatings through a modified hydrothermal method, and the resulting coating has demonstrated excellent osteointegration capability that outweighs many other coating systems for Ti based implants. An underlying property of such TiO_2/TiP hybrid coating would be its ability to induce photothermal heating under near infrared (NIR) laser irradiation,^[24] which arises from the wide bandgap (3.2 eV) and the strong NIR absorption ability of oxygen vacancies in TiO_2 .^[25] Compared to previously reported photothermal agents such as carbon-based nanomaterials (graphene,^[26] graphene oxide,^[27] carbon nanotubes^[28]) and gold nanoparticles,^[29] etc, our biocompatible photothermal conversion coating offers greater benefit in terms of biosafety. Although such promising property can be potentially deployed for a wide range of applications including photothermal therapies, it has never been exploited in the context of multifunctional bone scaffold.

Gelatin (Gel) is a denatured derivative of collagen that contains many functional amino acids and has been widely used in tissue engineering due to its bioaffinity, lack of antigenicity, and excellent cell attachment.^[30] Upon freeze drying, Gel presents a porous structure with pore size ranging from 50~600 μm .^[31] Literature suggests pores within 1~100 μm range are necessary for biomaterials as they mimic the typical pore size seen in porous bone structure, and 100~350 μm pores are optimum for bony ingrowth.^[32] It is hypothesized that combining 3D printed Ti scaffold and Gel could lead to a hybrid scaffold with hierarchical pore architecture that mimic the micro-environment of the natural bone, and hence facilitate new bone formation and ingrowth.

In this study, we designed and developed the first 3D-printed Ti6Al4V lattice scaffold with hydrothermally induced, photothermal conversion TiO_2/TiP coating (HR-Ti). The lattice scaffold was then infused with microporous drug laden Gel/hydroxyapatite composite hydrogel. The novel multifunctional hybrid scaffold with offers the major benefits in providing innovative approaches for

critical sized bone defect repair and serving as a novel platform for modulated osteosarcoma therapy.

2. Experimental section

2.1 Materials preparation

2.1.1 Preparation of drug-laden Gel/HA composite

Alendronate (ALN), is a commonly used bisphosphonate drug for osteoporosis management and bone regeneration.^[33] However, direct loading of ALN onto Gel often results in burst drug release due to the fast Gel degradation *in vivo*. In contrast, degradable HA microsphere is an excellent drug delivery vehicle, which can provide sustained/controlled drug release as well as promoting osteoblasts mineralization/maturation (due to slow release of Ca^{2+} and PO_4^{3-}).^[34] To prepare the ALN-laden HA microspheres/Gel composite (ALN-HA/Gel), HA microspheres were first synthesized following established procedure.^[35] 0.5 g ALN was then added into 50 mL aqueous dispersion containing 2.0 g HA microspheres. After mixing using shaking incubator under 37 °C for 48 h, ALN-HA were collected by centrifugation and vacuum dried at 40 °C for 24 h. ALN concentration in the supernatant solution was evaluated by UV-vis spectroscopy. The drug-laden Gel/ALN-HA can be obtained by dispersing 3.0g ALN-HA microspheres in 50 mL deionized water, followed by addition of 8.0 g Gel, and stirred magnetically at 1000 rpm under 50 °C for 1 h.

2.1.2 Preparation of 3D printed Ti6Al4V scaffolds

3D printed Ti6Al4V scaffolds (named as Ti) were manufactured by electron beam melting (EBM) facility in-house. The lattice structure was designed by computer-assisted design (CAD) software (Magics, Materialise, Belgium) based on a dodecahedron unit cell with strut diameter of 300 μm and porosity of 80%. Cubic scaffolds (5mm \times 5mm \times 5mm) were used for *in vitro* testing and cylindrical scaffolds ($\Phi = 6\text{mm}$, height = 6mm) were used for *in vivo* experiments. All samples were thoroughly cleaned by sonication in acetone, alcohol and deionized water for 30 min, respectively. The Ti scaffolds were subsequently subjected to hydrothermal treatment.^[36] Specifically, the scaffolds were immersed in an aqueous solution ($\text{m}(\text{H}_2\text{O}_2):\text{m}(\text{H}_3\text{PO}_4)$ 9:1) and placed in a Teflon-lined autoclave under 220 °C for 24 h. After the treatment, scaffolds were washed with distilled water and dried in air at room temperature for 24 h. The hydrothermally treated samples were named as HR-Ti.

2.1.3 Preparation of Gel/ALN-HA infused HR-Ti scaffold

The Gel/ALN-HA mixture was infused into the HR-Ti, then the infused scaffolds were held at -80 °C overnight followed by freeze-drying at -40 °C for 48 h. After that, the infused scaffolds were immersed in 100 mL ethanol containing 50mmol/L 1-ethyl-3-(3- (dimethylamino) propyl) carbodiimide hydrochlorid (EDC·HCl) and N-hydroxysuccinimide (NHS) at 4 °C for 10 h to crosslink the Gel content. Afterwards, the scaffolds were washed three times by ethanol and freeze-dried again. The final scaffolds were named as Gel/ALN-HA/HR-Ti. For comparison, ALN/HR-Ti (without Gel and HA), Gel/ALN/HR-Ti (without HA) and Gel/HA/HR-Ti (without ALN) were also prepared.

2.2 Materials characterization

2.2.1 Material characterization of microspheres

Morphology of the HA microspheres was observed by scanning electron microscopy (SEM, JSM-6510LV, JEOL, Japan) and transmission electron microscopy (TEM, JEOL-2000, Japan). The crystalline phase of the HA microspheres was characterized by X-ray diffractometer (XRD, DX-2500, China). The chemical composition of HA and ALN-HA microspheres was analyzed by EDS and X-ray photoelectron spectroscopy (XPS, AXIS Ultra DLD, USA). Fourier-transformed infrared spectroscopy (FTIR, Nicolet-6700, USA) was used in the wave number range of 400-4000 cm^{-1} to analyze the functional groups of HA and ALN-HA. To quantify the drug loading efficiency, thermogravimetric analysis (TG, STA449F3, Germany) was carried out in air in the temperature range 25-800 °C with a heating rate of 10 °C min^{-1} . Nitrogen adsorption-desorption isotherms (NADI) of HA and ALN-HA were measured using an automatic surface area and porosity analyzer (Kubo X1000, BUILDER, China). The pore volume and pore-size distributions were derived from the adsorption branches of the isotherms using the Barrett-Joyner-Halanda (BJH) method.^[37]

2.2.2 Material characterization of scaffolds

The structure and surface morphology of Ti, HR-Ti and Gel/ALN-HA/HR-Ti scaffolds were analyzed by stereoscope (SZX16/SZX10, Olympus, Japan) and SEM after gold sputtering. The scaffold surface elemental distribution was analyzed by EDS. In addition, compression tests (n=5) were carried out under ambient condition using Instron mechanical testing machine (Instron 5567, Instron Ltd., USA) at a loading rate of 1 mm/min.

2.2.3 *In vitro* degradation

Gel/ALN-HA/HR-Ti scaffolds were immersed in phosphate buffered solution (PBS, pH=7.2) at 37 °C for 28 days. The weight of the specimen was recorded at different time intervals (2 h, 4 h, 6 h, 8 h, 12 h, 1 d, 2 d, 3 d, 5 d, 7 d, 14 d, 21 d, 28 d). The weight loss (W_i) was calculated by comparing the initial weight (W_0) with the dried weight (W_d) following equation:

$$W_i \% = (W_0 - W_d) / W_0 \times 100\% \quad \text{Eq.1}$$

The surface morphology of scaffolds at different time interval was also observed by SEM.

2.2.4 *In vitro* drug release test

The ALN release behavior was studied by immersing drug-laded ALN/HR-Ti, Gel/ALN/HR-Ti and Gel/ALN-HA/HR-Ti in PBS solution (pH=7.2) at 37 °C for up to 28 days. The cumulative drug release was calculated at each predetermined time interval (2 h, 4 h, 6 h, 12 h, 1 d, 2d, 3 d, 5 d, 7 d, 14 d, 21 d, 28 d) using UV-vis spectroscopy following previously reported method.^[38]

2.2.5 *In vitro* photothermal response

HR-Ti and Gel/ALN-HA/HR-Ti were incubated in 48-well plate and their photothermal responses were captured when irradiated by 808 nm NIR laser in air and in immersed condition (400 μ L PBS), respectively. Light-induced temperature changes of the scaffolds at different laser power densities (0.25~1.5 W/cm²) were monitored by an infrared thermal imaging system (LWIRL808, Laserwave, Beijing, China) in real-time. The photothermal stability of the scaffolds were also investigated by irradiating the scaffolds over five LASER ON/OFF cycles.

2.3 *In vitro* osteogenic evaluation

2.3.1 Sample pretreatment

HR-Ti, Gel/HA/HR-Ti and Gel/ALN-HA/HR-Ti (5mm \times 5mm \times 5mm) were sterilized by low temperature plasma sterilizers (HRPS-120, Haier, Qingdao) for 2 h and stored in vacuum bag before testing. Isolation and culture of bone marrow mesenchymal stem cells (BMSCs) were carried out following standards ^[21] previously established by the Animal Research Committee of the State Key Laboratory of Oral Diseases and West China School of Stomatology, Sichuan University (approval number: SKLODLL2013A118).

2.3.2 Cell morphology observation

BMSCs at passage 2 (1.0×10^5 cells/mL) were seeded onto sterilized HR-Ti, Gel/HA/HR-Ti or Gel/ALN-HA/HR-Ti and incubated for 24 h. The cell-seeded scaffolds were rinsed three times with PBS to remove unattached cells, and the remaining cells were fixed for 4 h with 2.5% glutaraldehyde, followed by dehydration in graded ethanol solutions (20%, 40%, 60%, 80%, 90%, and 100%) and gold sputtered for SEM analysis. Another batch of parallel samples were permeabilized with 0.2% Triton X-100 (Sigma-Aldrich) for 15 min after fixing with 2.5% glutaraldehyde. Cell nuclei and cytoskeletons were stained with DAPI (blue fluorescence) and rhodamine-conjugated phalloidin (red fluorescence) for 20 min, respectively. Cell morphologies were then observed by a confocal laser scanning microscopy (CLSM, AIR MP⁺, Nikon, Japan).

2.3.3 Cell viability assay

The cell viability was assessed by Live/Dead staining and flow cytometry (FCM). Briefly, after 3 days of incubation, the cell viability on scaffolds was observed by staining live cells with Calcein AM and dead cells with Propidium iodide (Live/Dead Kit, Invitrogen, USA). Images of live (green) and dead (red) cells were scanned under inverted fluorescence microscope (TE2000-U, Nikon, Japan). In addition, cells cultured for 3 days were collected for FCM to further analyze the proportion of live and dead cells using flow cytometer (CytoFLEX LX, Beckman Coulter, USA) through combining cell Live/Dead staining with apoptosis kit (Solarbio, China). The assay was performed following the manufacturer's protocol, with blank cell culture being the control group.

2.3.4 Cell proliferation assay

After incubation with BMSCs (1×10^5 cells/well) for 1, 3, 5, and 7 days, the cell proliferation on HR-Ti, Gel/HA/HR-Ti and Gel/ALN-HA/HR-Ti was assessed using Cell Counting Kit (CCK-8, Beyotime, China) with blank cell culture plate being the control group. At different time interval (1d, 3d, 5d and 7d), the samples (n=3) were rinsed with PBS and incubated with 10% CCK-8 solution for 2 h at 37 °C. Finally, the absorbance was measured by a microplate reader (Thermo, USA) at 450nm.

2.3.5 ALP staining and activity assay

BMSCs (2×10^4 cells/well) were incubated for 1, 3, and 7 days on different samples. The culture was then fixed by 4% paraformaldehyde (Sigma-aldrich) and stained with an ALP kit (NBT/BCIP, Beyotime). After thorough washing the culture with deionized water, images were taken by light

microscopy (Olympus IX71, Tokyo, Japan). Optical density values for absorbance at 405 nm was measured to determine the ALP activity according to the manufacturer's protocol.

2.3.6 Cell immunofluorescence staining

After incubation with different scaffolds for 7 days, cells were fixed with 4% paraformaldehyde for 30 min and permeabilized with 0.2% Triton X-100 for 15 min. 4',6-diamidino-2-phenylindole and specific antibodies targeting the protein of interest (OCN and OPN) were added sequentially and co-incubated for 4 h as previously described.^[21] All procedures were completed in dark, and all samples were observed using CLSM after thorough rinsing using PBS.

2.3.7 Western blot assay

BMSCs (1×10^5 cells/well) were co-cultured with sterilized HR-Ti, Gel/HA/HR-Ti or Gel/ALN-HA/HR-Ti respectively for 7 days, and proteins were extracted by M-PER protein extraction reagent. The protein extract samples (20 μ g) were separated by 10% SDS-PAGE and transferred to polyvinylidene fluoride membranes. After blocked with 5% BSA in Tris-buffered saline/Tween 20 solution at room temperature for 2 h, membranes were incubated with different primary antibodies against Col-I, Runx-2, OCN and OPN overnight at 4 °C followed by HRP-labelled secondary antibody for 1 h under room temperature. The antibody-antigen reaction was detected with western blot analysis imaging system and the intensity of the protein bands was quantified on a western-light chemiluminescent detection system.

2.3.8 Quantitative real-time PCR analysis (qRT-PCR)

Cells incubated with sterilized HR-Ti, Gel/HA/HR-Ti or Gel/ALN-HA/HR-Ti (7 days) were collected for qRT-PCR tests to analyze the RNA expression of Col-I, Runx-2, OCN and OPN. The forward and reverse primers used in this study are listed in **Table S1**, and glyceraldehyde-3P-dehydrogenase (GAPDH) was used as the internal control gene. After 7 days of incubation, total cell RNA on different samples was extracted using TRIzol reagent according to the manufacturer's protocols, and reverse-transcribed into complementary DNA (cDNA) by using a Revert aid TM first strand cDNA synthesis Kit (Gibco, USA). Quantifications of selected genes were performed using real-time PCR with SYBR Premix Ex Taq (Takara).

2.3.9 Alizarin Red staining

Cells were seeded onto 24-well plates (1×10^5 cells/well). After 15-day incubation, cells were fixed in ice-cold 95% ethyl alcohol for 10 min and stained with 2% Alizarin Red Staining solution (pH = 4.2) for 30 min. After thorough cleaning with deionized water, the cell images were taken using an inverted fluorescence microscope. All analyses were performed independently in triplicate.

2.4 *In vitro* photothermal ablation of osteosarcoma cells

Osteosarcoma cells (MG-63, 1×10^4 cells/well) were seeded in 24 well plates, and HR-Ti, Gel/HA/HR-Ti or Gel/ALN-HA/HR-Ti scaffolds were placed gently into the seeded plates. The scaffolds were then irradiated with NIR laser (1.5 W/cm^2) for different duration (0, 2, 4, 6, 8, 10 min) and CCK-8 assay was carried out to evaluate the *in vitro* MG-63 ablation efficiency. Blank cell culture plate was used as the control group.

CLSM was used to observe the cytoskeleton of cells on different samples with or without photothermal treatment. The medium was removed after the treatment and the adherent cells were rinsed with PBS. The cytoskeleton and nuclei were stained with rhodamine phalloidin and DAPI for 30 min at 37 °C, respectively. Additionally, Live/Dead assay has also been carried out on different scaffolds with or without laser irradiation.

2.5 *In vivo* animal studies

2.5.1 Surgical procedures

The animal studies were performed in compliance with the international guidance on animal welfare and the standards of the Animal Research Committee of the State Key Laboratory of Oral Diseases and West China School of Stomatology, Sichuan University (approval number: WCCSIRB-D-2014-407). Eighteen adult New Zealand white rabbits (~ 3.0 kg/each) were randomly assigned into three groups for 4, 8 or 12 weeks implantation of sterilized HR-Ti, Gel/HA/HR-Ti or Gel/ALN-HA/HR-Ti and the blank control, respectively. Scaffold was inserted into the bone defect ($\Phi 6\text{mm} \times 6\text{mm}$) created in medial condyle by press fitting, see **Fig. S11**. The soft tissues were then sutured, and intramuscular injection of penicilin was administered for 3 consecutive days post-surgery.

2.5.2 Micro-computerized tomography evaluation (Micro-CT)

4, 8 or 12 weeks after implantation, three femur samples with implants in each group were harvested and evaluated by Micro-CT ($\mu\text{-CT80}$, Scanco Medical, Switzerland). 3D models of the

femur as well as that of the local implantation site were reconstructed using CT Vol program (Sky scan Company). The quantitative evaluation of osteogenesis such as bone volume per total sample volume (BV/TV), trabecular number (Tb. N), trabecular thickness (Tb. Th) and trabecular separation (Tb. Sp) were obtained by the Direct Method software. A cylindrical region of interest (ROI with the same size as the bone defect) was selected to characterize the new bone formation inside the scaffold.

2.5.3 Histological analysis

The harvested samples were fixed by 4% buffered paraformaldehyde, dehydrated using graded ethanol solution (70%, 85%, 95% and 100%), and embedded in methyl methacrylate without decalcification. Samples were then microtomed into 5 μm thick slices along the cross-sectional surface, stained by methyl blue and basic fuchsin and observed under optical microscopy (Leica DMI 6000B, Leica SP, Germany).

2.5.4 Biomechanical test

Rabbit femur specimens with implants (n=3) were harvested 12 weeks post-operation for biomechanical testing using a universal testing machine (BSC30, Yinbo Scientific Equipment, China). The samples were subjected to push-out tests at a loading rate of 1 mm/min with the maximal load value representing the push-out force between the implant and the bone tissues.

2.6 Statistical analysis

Statistical analysis was performed using SPSS software, and the statistical significance was analyzed using one-way analysis of variance (ANOVA) followed by the LSD *post hoc test*. Statistical significance was considered for $p < 0.05$, while high significance was $p < 0.01$.

3. Results and discussion

3.1 Materials characterization

3.1.1 Characterization of microspheres

Hollow HA microspheres with the average diameter of $\sim 1.2 \mu\text{m}$ have been successfully synthesized, see **Fig. S1** and **Fig. S2**. The NADI curve of HA microspheres (**Fig. 1A**) features type IV isotherms with type H3 hysteresis loop. Results show that HA microspheres have a specific surface area of $154.8 \text{ m}^2 \cdot \text{g}^{-1}$, a pore volume of $0.43 \text{ cm}^3 \cdot \text{g}^{-1}$ and average pore size of 7.02 nm. The large specific surface area, pore volume and mesoporous structure of the as synthesized HA

microspheres make them the ideal platform for drug delivery. [39] After drug loading, the microspheres specific surface area, pore volume and the average pore size decreases to $122.3 \text{ m}^2 \cdot \text{g}^{-1}$, $0.37 \text{ cm}^3 \cdot \text{g}^{-1}$ and 4.77 nm , respectively (see **Fig. 1B**), suggesting adsorption of ALN onto microspheres. The successful drug loading can be further corroborated by the presence of N characteristic peak in the EDS (**Fig. S3**) and XPS (**Fig. 1C**) spectra. TGA analysis in **Fig. 1D** shows that a drug loading efficiency of 29.0% has been achieved.

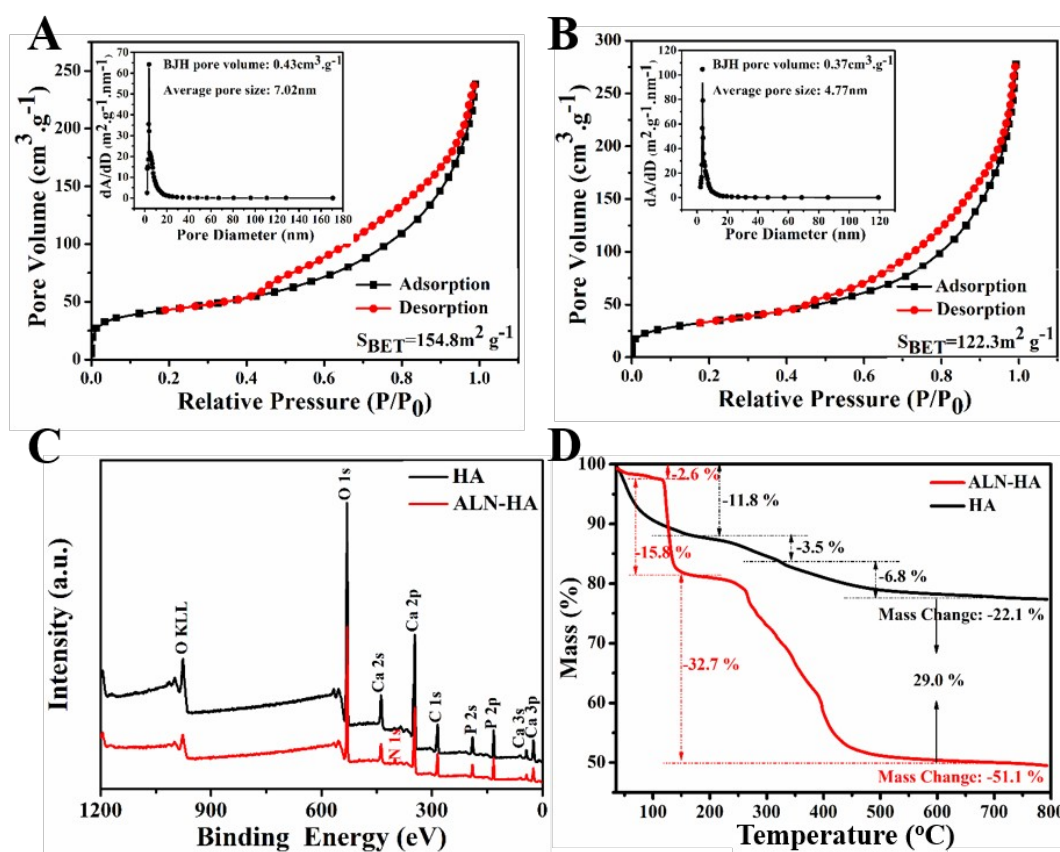


Fig. 1. NAD₂ curve of HA (A) and ALN-HA (B); XPS spectra (C) and TG curves of HA and ALN-HA microspheres.

3.1.2 Characterization of scaffolds

Fig. 2A and **2B** shows the structure of Ti and HR-Ti scaffolds. Both Ti and HR-Ti present a lattice structure with uniform strut spacing. Ti has a relatively smooth strut surface (**Fig. 2A(b)**), whereas HR-Ti is covered by coating featuring randomly arranged nanorods (**Fig. 2B(b)**). Previous literature suggests the HR coating mainly consists of Ti, TiO₂, crystalline Ti(HPO₄)₂ and (TiO)₂P₂O₇.

[40] The detailed coating elemental information of Ti and HR-Ti is shown in the EDS spectra (**Fig. 2C**

and **2D**).

Fig. 3 A shows the stereoscopic image and SEM images of the Gel/ALN-HA/HR-Ti. It can be seen that after Gel/ALN-HA infusion, the interior and exterior of HR-Ti scaffold are well covered by colloidal substance with porous structure. **Fig. 3A(b)** reveal that Gel/ALN-HA/HR-Ti features a hybrid architecture consisting of 3D printed HR-Ti lattice with interpenetrating Gel/ALN-HA. Gel has a pore size 50~600 μm , similar to the porous structure of extracellular matrix (ECM), and is expected to promote the ingrowth of BMSCs. ^[41] Under high magnification SEM images, HA microspheres are found to be incorporated into the Gel. EDS analysis (**Fig. S4**) and elemental mapping (**Fig. 3B**) show the presence of Ca, C, N, Na, which confirms the even distribution of ALN over the entire scaffold.

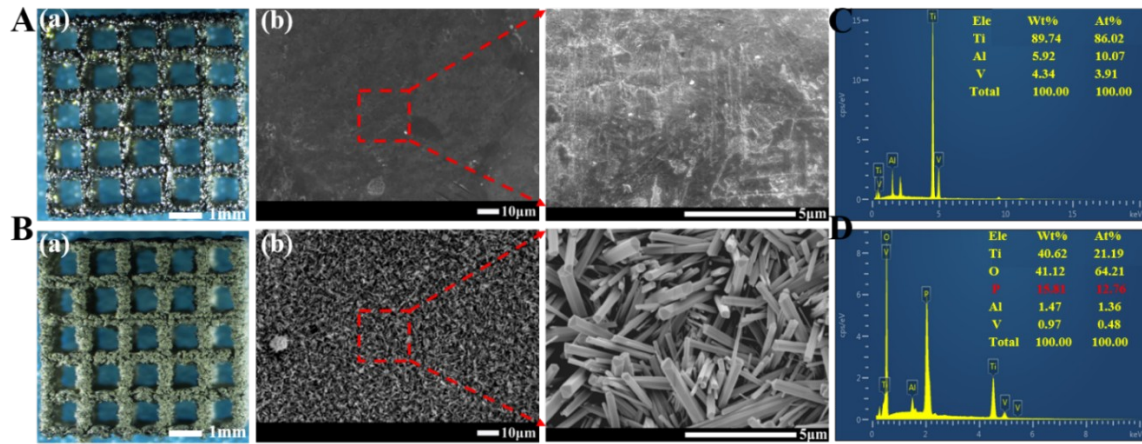


Fig. 2. Stereoscopic images (a) and SEM images (b) of Ti (A) and HR-Ti (B); EDS spectra of Ti (C) and HR-Ti (D).

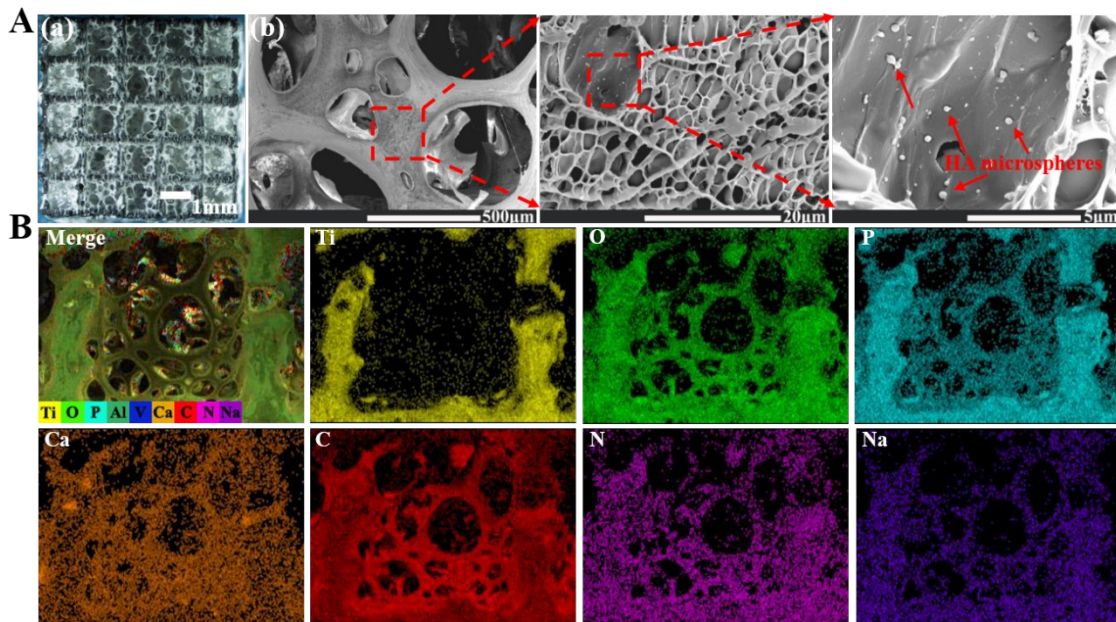


Fig. 3. (A) Stereoscopic image (a), SEM images (b) and the EDS images (B) showing elemental mapping of Gel/ALN-HA/HR-Ti.

Fig. 4A shows the typical stress-strain curves obtained for three different scaffolds during compressive tests. **Fig. 4B** shows that the initial compressive strength of HR-Ti increases slightly from 14.4 ± 1.7 MPa to 16.2 ± 2.1 MPa and 17.8 ± 1.6 MPa, respectively, after infusing with Gel/HA and Gel/ALN-HA. The associated scaffold elastic moduli increases from 5.2 ± 0.2 GPa to 8.2 ± 0.3 GPa and 8.8 ± 0.2 GPa, respectively. The mechanical properties shown by these scaffolds are comparable to that of the human bone. The increased compressive strength and elastic modulus seen

in the Gel/HA/HR-Ti and Gel/ALN-HA/HR-Ti may be attributed to the penetration of the organic/inorganic composites (Gel/HA) into the HR-Ti scaffold interior (and into the microporous TiO₂/TiP coating), further reinforcing the structure.

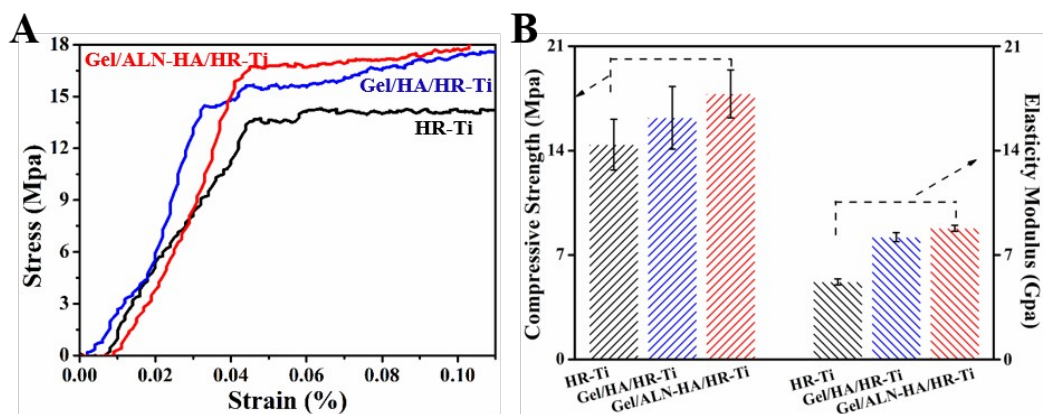


Fig. 4. Compressive stress-strain curves (A) and the associated data (B) of HR-Ti, Gel/HA/HR-Ti and Gel/ALN-HA/HR-Ti.

3.1.3 *In vitro* degradation and drug releasing behavior

The *in vitro* degradation of Gel/ALN-HA/HR-Ti has been characterized in terms of morphological/structural changes and the corresponding weight loss. As is shown in SEM images in **Fig. 5A**, the Gel matrix that cover the scaffold surface starts to degrade 4 h after immersion, exposing partial HR-Ti struts surface. 12 h after immersion, Gel/ALN-HA further degrades into ribbon-like strips, the macropores and struts of the HR-Ti become more visible. After 1 day, the Gel matrix on the scaffold strut surface mostly degrades, however the Gel matrix within the scaffold lattice macropores only degrade completely by day 28. The degradation results can be further corroborated by the scaffold weight loss curve shown in **Fig. 5B**. The Gel/ALN-HA/HR-Ti shows a more drastic weight loss (~10%) in day 1, followed by more gradual weight loss from day 4 onwards. The residual weight measured on day 28 (1.3508g) is very close to the original weight of HR-Ti (1.3502g), implying complete degradation of the Gel matrix, which is consistent with the SEM observation. **Fig. 5C** shows the drug release curves for ALN/HR-Ti, Gel/ALN/HR-Ti and Gel/ALN-HA/HR-Ti immersed in PBS solution at 37 °C for 28 days. ALN/HR-Ti shows a typical burst release behavior, with > 90% ALN released in the first 2 days. The remaining drug was released completely by day 5, indicating the nanostructured TiP coating on HR-Ti does not support sustained

drug release under physiological conditions. For Gel/ALN/HR-Ti, an initial release of $\sim 50\%$ is seen for the first 2 days. The drug release curve plateaus from day 7 and a total release is achieved by day 28.

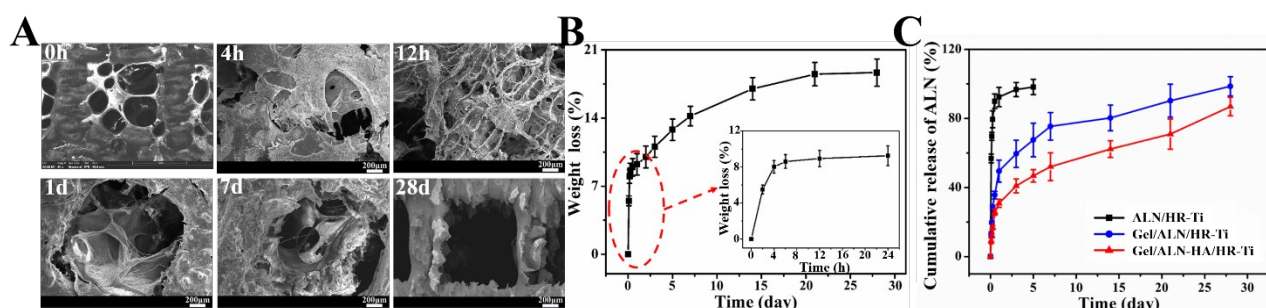


Fig. 5. (A) SEM images showing gradual degradation of Gel/ALN-HA/HR-Ti when immersed in PBS; (B) weight loss of Gel/ALN-HA/HR-Ti during the 28d immersion period and (C) cumulative releasing ALN from ALN/HR-Ti, Gel/ALN/HR-Ti and Gel/ALN-HA/HR-Ti.

In contrast, Gel/ALN-HA/HR-Ti shows the slowest ALN releases ($\sim 30\%$) in the initial 2 days, followed by steady drug release up to day 28 (cumulative release $\sim 78\%$). This is because the mesoporous HA microspheres provide additional physical barrier, which further slows down the drug elution. Even after the complete Gel degradation, 22% of ALN still remain. This is because HA microspheres have a much slower degradation rate than Gel.^[42] Upon complete Gel degradation, there were still residual HA microspheres (carrying unreleased ALN) being released into the surrounding PBS, contributing to the more sustained drug release profile.

3.1.4 Photothermal effect of scaffolds

Fig. 6A and **6B** show that HR-Ti and Gel/ALN-HA/HR-Ti exhibit strong photothermal response under irradiation of 808 nm NIR under both ambient and immersed (PBS) conditions. The strong NIR absorbance and high photothermal conversion efficiency of the scaffold can be attributed to the wide bandgap (3.2 eV) and the oxygen vacancies of TiO_2 within the HR induced coating.^[27, 28] **Fig. 6C** and **6D** suggest that the photothermal conversion efficiency of the scaffolds are dependent on the laser power, irradiation time, and the surrounding medium. In contrast, the scaffold chemical composition does not seem to have significant influence on the photothermal response. For instance, with laser power $> 1 \text{ W/cm}^2$, both scaffolds can reach temperature $> 45 \text{ }^\circ\text{C}$ (i.e., therapeutic window for cancer therapy) within 50 s under ambient condition. The curve then plateaus, indicating stabilization of the temperature with time. Further increasing the NIR laser power can accelerate the

heating process (e.g., reaches 45 °C within 25 s for 1.5 W/cm²). When the scaffolds are immersed in PBS, the laser heating effect has been attenuated due to the heat dissipation into the surrounding medium. The most effective laser power is 1.5 W/cm² and both scaffolds can reach 45 °C within 200s in PBS. **Fig. S5** shows that under repeated laser irradiation, the photothermal performance of HR-Ti and Gel/ALN-HA/HR-Ti do not deteriorate, demonstrating their excellent thermal stability in repeated photothermal applications.

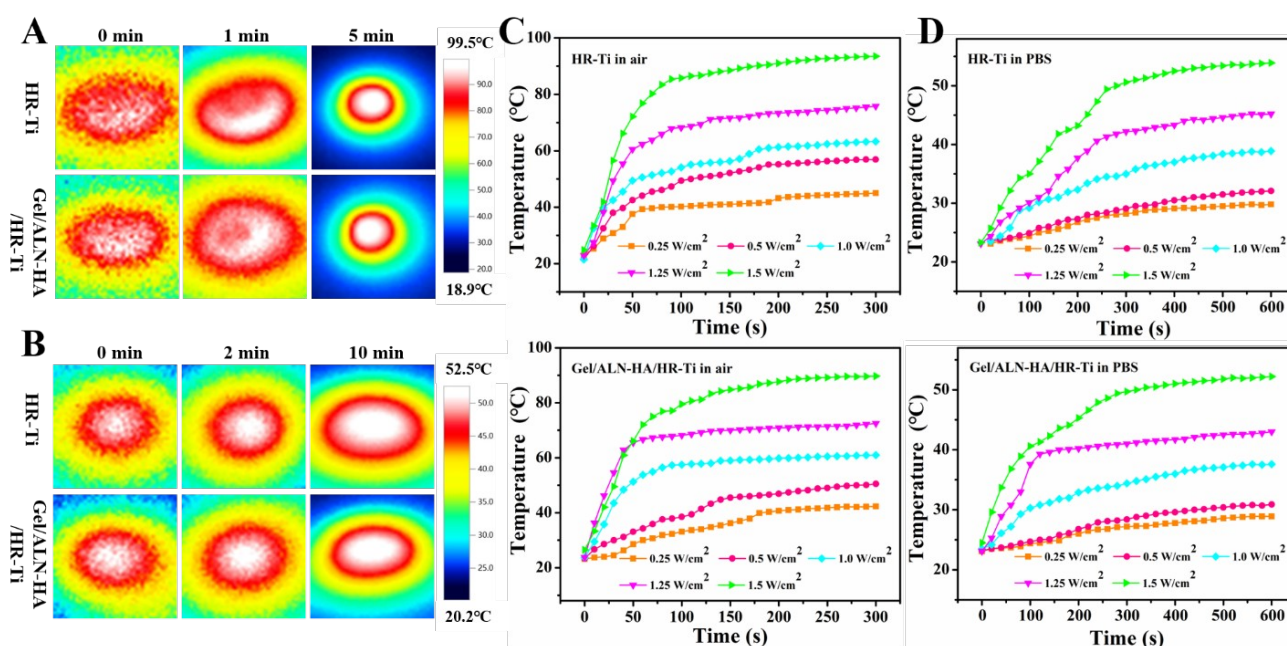


Fig. 6. Thermal images of HR-Ti and Gel/ALN-HA/HR-Ti in air (A) and in PBS (B) under 808 nm laser irradiation (1.5 W/cm²); temperature profile of HR-Ti and Gel/ALN-HA/HR-Ti under irradiation of different laser power densities in air (C) and in PBS (D).

3.2 *In vitro* studies

3.2.1 Biocompatibility assessment

BMSCs adhesion and morphologies on different scaffolds are investigated by SEM and CLSM after 24 h incubation (**Fig. S6**). SEM images in **Fig. S6A** confirm the adhesion of BMSCs on HR-Ti, Gel/HA/HR-Ti, and Gel/ALN-HA/HR-Ti samples, suggesting all three types of scaffolds are all conducive to cell adhesion. However, compared to HR-Ti, Gel/HA/HR-Ti and Gel/ALN-HA/HR-Ti surface exhibit greater cell densities, indicating that the introduction of Gel/HA or Gel/HA-ALN favors cell adhesion. CLSM images in **Fig. S6B** shows more clearly organized cytoskeletons. Cells attached on the three samples feature spindle shapes, longer filopodia and cytoplasmic extensions, suggesting variation in material compositions has no negative effect on the growth of BMSCs.

The cell viability on HR-Ti, Gel/HA/HR-Ti and Gel/ALN-HA/HR-Ti on day 3 are assessed by Live/Dead staining and flow cytometry analysis. The fluorescence staining images in **Fig. 7A** show that all groups exhibit large amount of cells attachment and survival, indicating all the three scaffolds have no cytotoxicity against the control. The results can be further confirmed by FCM analysis shown in **Fig. 7B**, in which the top left values represent the proportion of dead cells while the bottom right values represent the proportion of live cells. The numeric values of live cells cultured with all three scaffolds are over 80% with no significant difference from the control group.

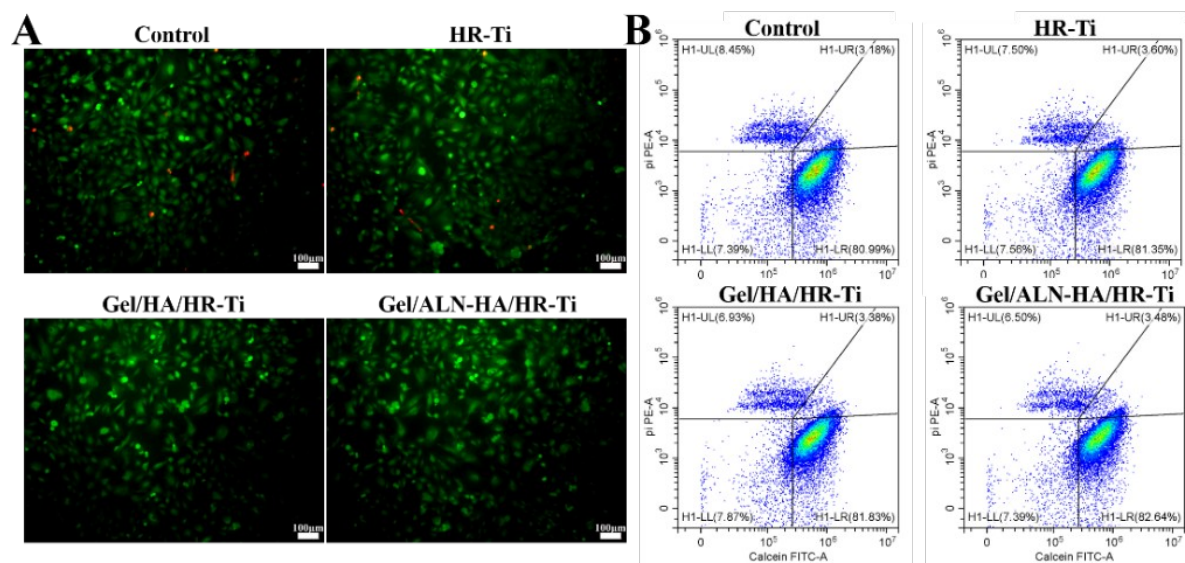


Fig. 7. The Live-Dead fluorescence images (A) and FCM analysis (B) for BMSCs cell viability after 3d incubation with different scaffolds.

Cell proliferation measured by CCK-8 assay is shown in **Fig. 8A**. It can be seen that all groups show a sustainable proliferation over time, confirming the scaffolds under investigation possess excellent biocompatibility. In particular, Gel/HA/HR-Ti and Gel/ALN-HA/HR-Ti exhibit a higher level of cell proliferation than the HR-Ti and the control groups during the 7d co-culture cycle, especially for 5~7 d ($p < 0.05$).

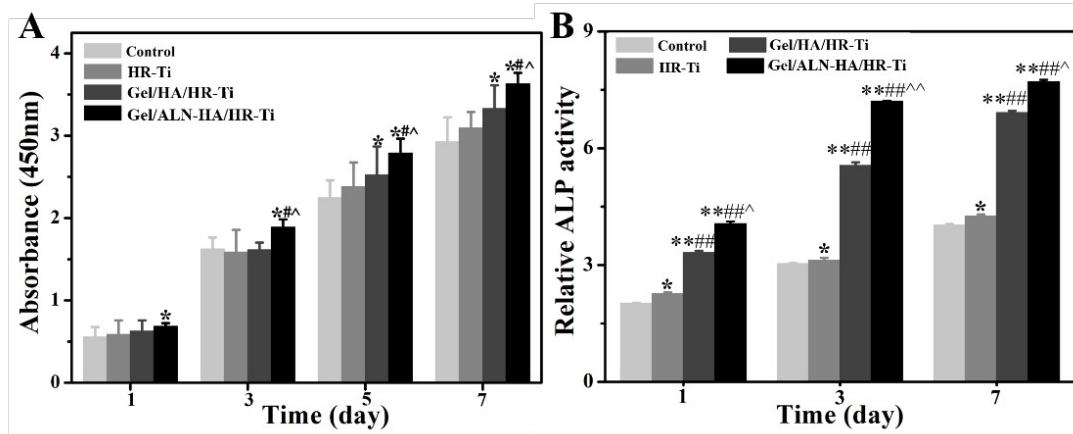


Fig. 8. The cell proliferation (A) and the relative ALP activity (B) of BMSCs incubated on different scaffolds over a 7d period, * $p < 0.05$, ** $p < 0.01$ vs control; # $p < 0.05$, ## $p < 0.01$ compared vs HR-Ti; ^ $p < 0.05$, ^^ $p < 0.01$ compared vs Gel/HA/HR-Ti.

The results indicate that the incorporation of bionic components (Gel/HA) into the scaffold provide a local signal transmission link between implant and adherent cells, thereby promoted the BMSCs adhesion and proliferation.^[43] Furthermore, the interpenetrating porous Gel/HA structure in scaffold interior also provides favorable support for BMSCs adhesion and mineralization. For Gel/ALN-HA/HR-Ti, the presence of ALN could also partially contribute to the high proliferative activity, as the drug can inhibit bone resorption (by inhibiting osteoclast proliferation) and promote osteoblast growth and differentiation.^[44]

3.2.2 Differentiation of BMSCs

The early osteogenic ability of BMSCs has been evaluated using Alkaline phosphatase (ALP) as an early osteogenic marker. **Fig. S7** shows that significant increase in bluish violet compounds can be observed for Gel/HA/HR-Ti and Gel/ALN-HA/HR-Ti as compared to the control and the HR-Ti group. Statistical analysis from results in **Fig. 8B** suggests that the quantitative ALP activity of cells cultured with HR-Ti during 1~7 d is greater than that of the control group ($p < 0.05$). This can be due to the nano-rod like TiP coating providing a bio-mimic structure similar to the osteoclast-resorbed human bone surface, which is highly conducive to cell regulation. On the other hand, the presence of bioactive element P also favors BMSCs differentiation and bone regeneration.^[45] Compared to the control and the HR-Ti group, Gel/HA/HR-Ti and Gel/ALN-HA/HR-Ti exhibit much enhanced ALP activity ($p < 0.01$), with cells on Gel/ALN-HA/HR-Ti showing the highest ALP activity value ($p <$

0.01) at each time point. Additionally, increased expression of OCN and OPN are also observed for all groups, see **Fig. S8**. OCN and OPN are two important indices in bone remodeling, and they are associated with the osteogenic function and the new bone construction/mineralization, respectively. [46] Similar to the ALP activity assay, a much stronger fluorescent intensity can be seen for fluorescence-stained cells on Gel/HA/HR-Ti and Gel/ALN-HA/HR-Ti (**Fig. S8**), and Gel/ALN-HA/HR-Ti shows the most abundant OCN and OPN expression, indicating its great potential in bone regeneration.

The expression of four representative osteogenic genes (Col-I, Runx-2, OCN, OPN) was also measured *via* western blot and qRT-PCR on day 7, see **Fig. 9**. Col-I is regarded as the marker for BMSCs osteogenesis. [47] Runx-2, a core-binding protein factor, is a key transcription factor associated with osteoblastic differentiation. [48] Results in **Fig. 9A** and **9B** both indicate a significantly up-regulated expression of the four osteogenic genes for cells cultured with Gel/HA/HR-Ti and Gel/ALN-HA/HR-Ti when compared with the control and the HR-Ti group ($p < 0.01$). Among all groups, cells seeded on Gel/ALN-HA/HR-Ti exhibit the highest expression level ($p < 0.05$ or $p < 0.01$). This could be due to the combined effect of the presence of bionic component (Gel/HA), the sustained release of ALN and the favorable microstructure of Gel/ALN-HA/HR-Ti.

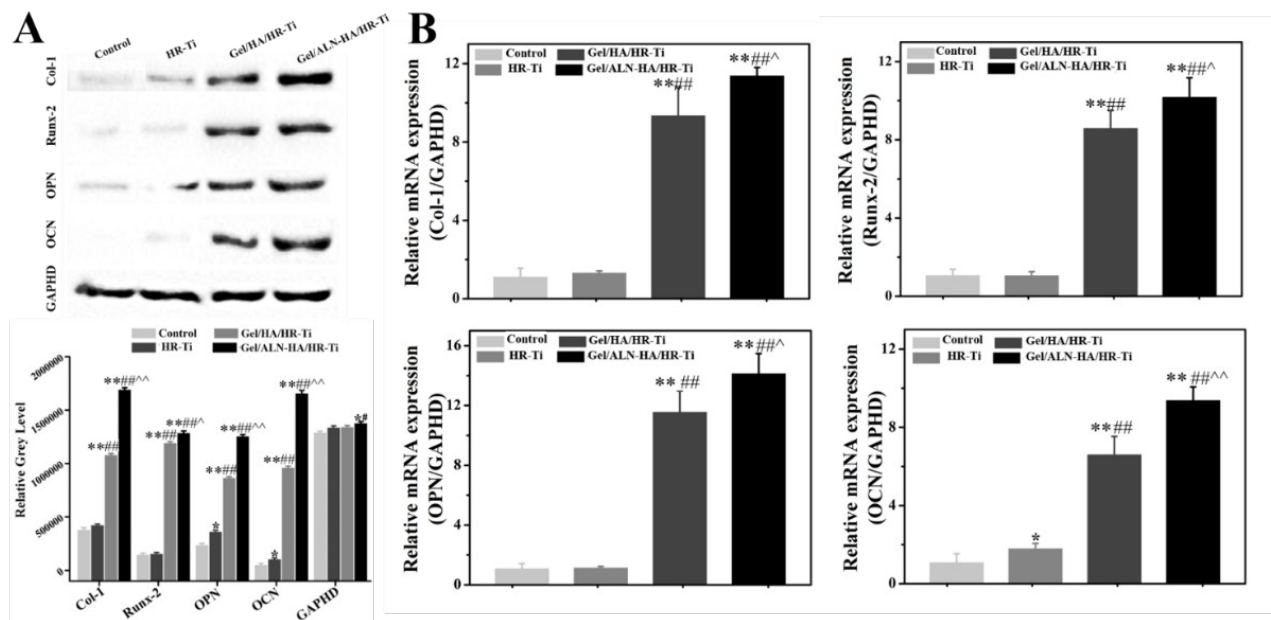


Fig. 9. Western blot assay on Col-I, Runx-2, OCN and OPN for qualitative and quantitative detection of initial cell adhesion and osteoblastic differentiation (A); the mRNA expression levels of various osteogenic factors determined

by qRT-PCR (B), * $p < 0.05$, ** $p < 0.01$ vs control; # $p < 0.05$, ## $p < 0.01$ compared vs HR-Ti; ^ $p < 0.05$, ^ $p < 0.01$ compared vs Gel/HA/HR-Ti.

Alizarin red staining was used to detect the osteogenic differentiation of scaffolds on day 15. ^[49] As shown in **Fig. S9**, in comparison to the control and the HR-Ti group, a significant higher level of dark red Ca deposition can be observed in Gel/HA/HR-Ti and Gel/ALN-HA/HR-Ti. In particular, BMSCs cultured with Gel/ALN-HA/HR-Ti are almost completely covered by mineralized Ca nodules, indicating Gel/ALN-HA/HR-Ti is most favorable for late osteogenic BMSCs differentiation.

3.3 In vitro photothermal ablation of bone tumor cells

The photothermal conversion function of our scaffolds for potential cancer ablation (osteosarcoma cells, MG-63) has been investigated. It can be seen from **Fig. 10A** that MG-63 cells show distinct proliferation in all groups without NIR laser irradiation. In contrast, 10 min laser irradiation at a power density of 1.5 W/cm^2 can lead to significant reduction in cell viability (~57 % reduction vs control) on HR-Ti, Gel/HA/HR-Ti and Gel/ALN-HA/HR-Ti ($p < 0.01$). There is no significant difference in the cancer ablation efficiency amongst the three experimental groups. Additional experimental data for Gel/ALN-HA/HR-Ti confirms the viability of MG-63 gradually decreases with increasing laser irradiation time (**Fig. 10B**).

CLSM images reveal the morphology and cytoskeleton of MG-63 cells on different scaffolds (**Fig. S10A**). Before NIR laser irradiation, MG-63 cells are well spread and present active morphology with affluent pseudopods in all groups. After 10 min of laser irradiation, few MG-63 cells can be found in the experimental groups, and the cell pseudopods disappear. Live/Dead assay in **Fig. S10B** confirm near total ablation of MG-63 cells on all experimental groups after 10 min laser treatment.

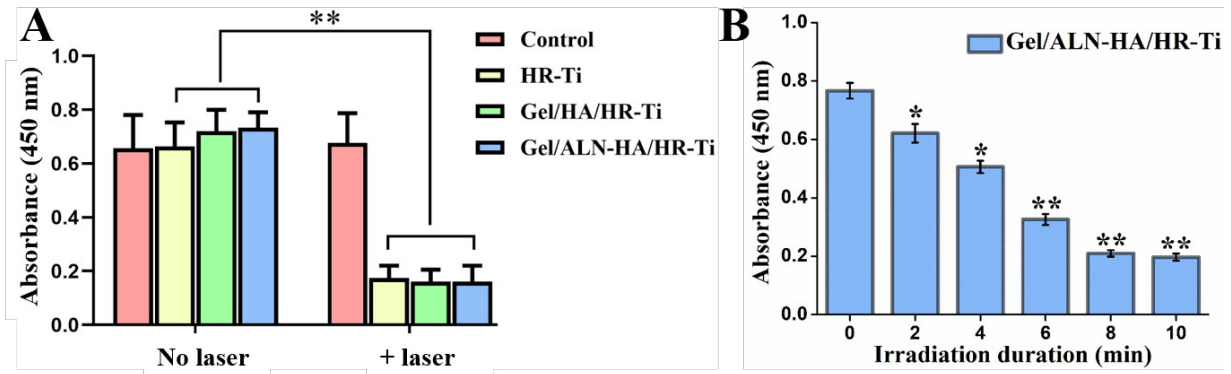


Fig. 10. Proliferation of MG-63 cells on different groups for 1 d (A); the proliferation viability of MG-63 cells treated with Gel/ALN-HA/HR-Ti for different irradiation durations (B); * $p < 0.05$, ** $p < 0.01$ vs control.

3.4 *In vivo* osteointegration

The rabbit femoral specimens harvested 12 weeks post-surgery are shown in **Fig. 11A**. All the scaffold implants remain well-positioned inside the distal femur without obvious complications (such as congestion, degeneration, necrosis, abscesses, or infections) around the implantation site. The osteogenesis capacities of different samples are further evaluated by 3D Micro-CT reconstruction images, see **Fig. 11B** and **C**. All four groups show an increasing growth of new bone over time, see **Fig. S12** and **S13**. By week 12, all four groups showed clear osteogenesis, while the new bone formation of Gel/HA/HR-Ti and Gel/ALN-HA/HR-Ti are much greater than that of the control and the HR-Ti group. More extensive bone regrowth and much denser bone matrix was observed on the exterior and the interior of the Gel/ALN-HA/HR-Ti scaffold, which coincides with the scaffold's strong ability in inducing cells adhesion and infiltration. The quantitative assessments on new bone volume (BV), trabeculae number (Tb.N) and thickness (Tb.Th) shows all three indices follow the order: Gel/ALN-HA/HR-Ti > Gel/HA/HR-Ti > HR-Ti > control, whereas trabeculae separation (Tb.Sp) data shows an reverse trend: Gel/ALN-HA/HR-Ti < Gel/HA/HR-Ti < HR-Ti < control 12 weeks post-surgery (**Fig. 11D**). The data suggest that the Gel/ALN-HA/HR-Ti possesses the best osteogenic capability and is the most favorable candidate for bone defect repair.

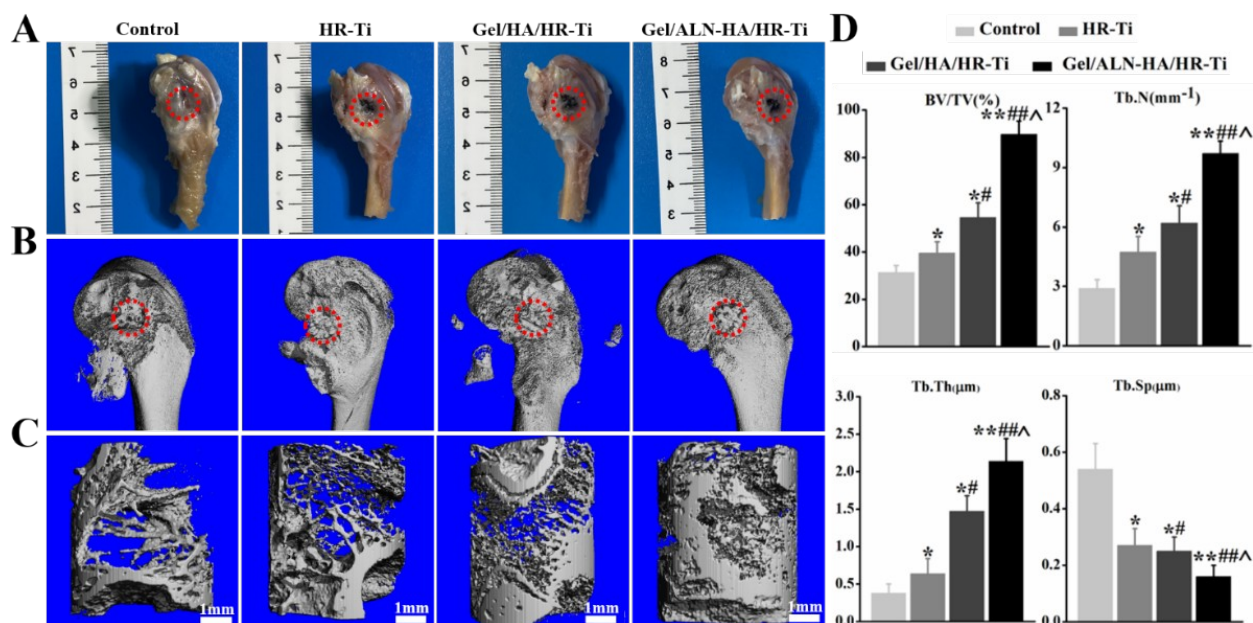


Fig. 11. Images exhibiting the excised scaffolds with surrounding tissue (A); three-dimensional Micro-CT reconstruction images (B); Micro-CT reconstruction images representing newly formed bone tissues (C) and the quantitative analysis of osseointegration (D) of different groups at 12 weeks after surgery, * $p < 0.05$, ** $p < 0.01$ vs control; # $p < 0.05$, ## $p < 0.01$ compared vs HR-Ti; ^ $p < 0.05$, ^^ $p < 0.01$ compared vs Gel/HA/HR-Ti.

Fig. 12 shows the methylene blue-basic fuchsin stained histological images of implant cross-section in the femoral condyle defects 12 weeks post-surgery. For the control group, only little new bones tissue can be found scattered in the defect site. For HR-Ti, slightly increasing amount of mineralized new bone can be found in the peripheral area of the scaffold, without much evidence of bone ingrowth. In contrast, significantly new bone in-growth has been observed for Gel/HA/HR-Ti and Gel/ALN-HA/HR-Ti. For Gel/ALN-HA/HR-Ti in particular, the scaffold struts are well surrounded by new bones forming a mechanically interlocked structure, and its new bone mass is much greater than other groups, consistent with the Micro-CT results.

12 weeks post-surgery, pull-out experiments were performed to analyze the interfacial bonding between the implants and the surrounding bone tissues. **Fig. 13** shows the typical displacement curves and the average push-out force. The average maximum push-out force obtained from HR-Ti, Gel/HA/HR-Ti and Gel/ALN-HA/HR-Ti are 159.7 N, 426.2 N and 530.7 N, respectively. The push-out force of Gel/ALN-HA/HR-Ti is significantly higher than the Ti based implants reported in the previous literature (e.g., ~174N,^[50] ~200N,^[21] ~480N^[51]).

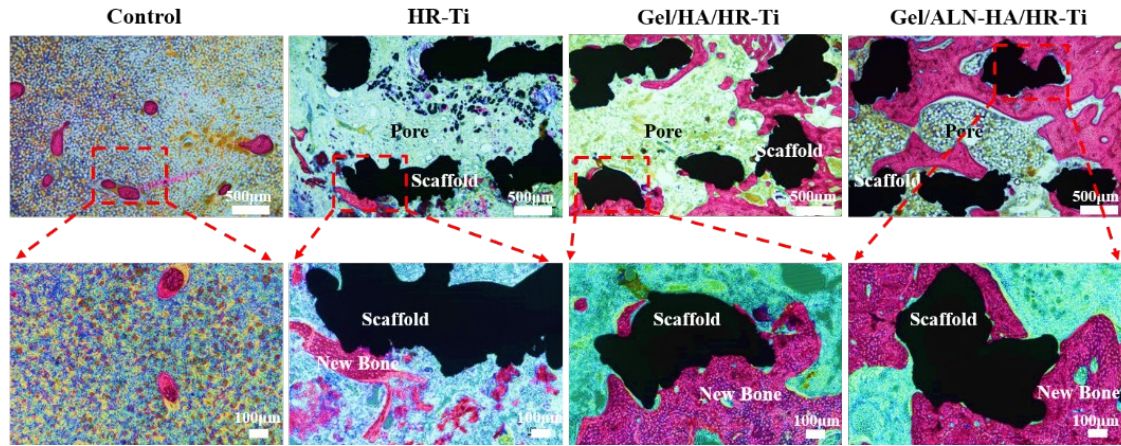


Fig. 12. Methylene blue basic fuchsin stained histological sections of bone tissue for different groups 12 weeks post-surgery (Black: implant struts, Pink: new bone).

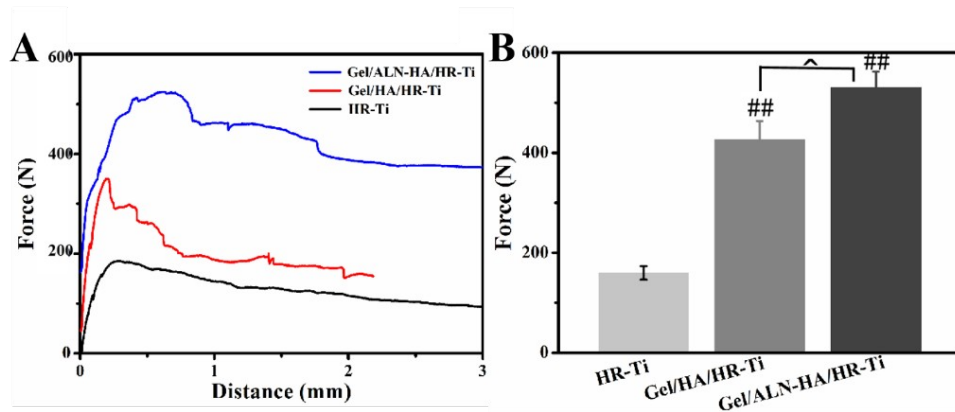


Fig. 13. The force-displacement curves (A) and the maximum push-out forces (B) of different scaffolds 12 weeks post-surgery, ## $p < 0.01$ compared vs HR-Ti; ^ $p < 0.05$ compared vs Gel/HA/HR-Ti.

4. Conclusions

This study describes the successful design and construction of the first Ti6Al4V based hybrid bone scaffold based on a combination of 3D printing technology, photothermal conversion coating, and incorporation of drug laden Gel/HA nanocomposite. The hybrid scaffold system can offer the major benefits such as (1) allowing be-spoke geometry specific to the bone defect, (2) providing tailed mechanical properties similar to that of the natural bone, (3) enabling on-demand localized photothermal conversion for bone cancer ablation and (4) providing ideal hierarchical microstructure as well as sustained release of bone-regenerative medicine, promoting cell adhesion and bone re-growth. It is envisaged that the new scaffold technology holds a strong promise in vital applications in bone repair and broader biomedical applications such as management of bone cancer,

osteomyelitis, etc, and therefore would play an important role in reducing cost in the healthcare industry as well as improving the patients' quality of life.

* Corresponding authors

Li Zhang, Email: nic1976@scu.edu.cn or zhangli9111@126.com

Ganjun Feng, Email: gjfenghx@163.com

Yubao Li, Email: nic7504@scu.edu.cn

Contributions

L. Zhang, D. Sun, G. J. Feng and B. Y. Cai conceived ideas of this work. B. Y. Cai carried out all experimental work in relation to materials preparation and characterization. J. C. Wang. performed the cytology-related work and L. Z. Huang undertook the *in vivo* animal experiments. All authors contributed to the data analysis, discussion as well as the writing and revision of the manuscript.

Conflicts of interest

There are no conflicts of interest to declare.

Acknowledgements

We would like to thank Shanling Wang, Jiqui Wen, Suilin Liu, and Li Chen (Analytical & Testing Center, SCU) for their help with TEM, XRD, XPS and Micro-CT testing, respectively. This work was also supported by the National Key Research and Development Program of China (2016YFA0201703), National Natural Science Foundation of China (52001324, 81772397, 82072434) and National Science Foundation of Jiangsu Province (BK20200643).

References

1. Luca A D, Raimondi L, Salamanna F, et al. Relevance of 3d culture systems to study osteosarcoma environment. *J. Exp. Clin. Cancer*, 2018, 37(1): 2-16.
2. Zhao X Y, Han Y, Sun Y, et al. Combining photothermal ablation-based vaccine with immune checkpoint blockade for synergistic osteosarcoma immunotherapy. *Mater. Des.*, 2021, 198(3): 109311.
3. Ferrari S. Postrelapse survival in osteosarcoma of the extremities: prognostic factors for long-term survival. *J. Clin. Oncol.*, 2003, 21(4): 710-715.
4. Roundhill E A, Jabri S, and Burchill S A. ABCG1 and Pgp identify drug resistant, self-renewing osteosarcoma cell. *Cancer Lett.*, 2019, 453: 142-157.

5. Wernike E, Montjovent M O, Liu Y, et al. VEGF incorporated into calcium phosphate ceramics promotes vascularization and bone formation in vivo. *Eur. Cell Mater.*, 2010, 19(1): 30-40.
6. Emeka N, Neukam F W. Autogenous bone harvesting and grafting in advanced jaw resorption: morbidity, resorption and implant survival. *Eur. J. Oral Implantol.*, 2014, null: S203-217.
7. Yang Y W, He C X, E D Y, et al. Mg bone implant: features, developments and perspectives. *Mater. Des.*, 2020, 185(5): 108259.
8. Sun H, Hu C, Zhou C C, et al. 3D printing of calcium phosphate scaffolds with controlled release of antibacterial functions for jaw bone repair. *Mater. Des.*, 2020, 189: 108540.
9. Ghayor C, Bhattacharya L, Weber F E, et al. The optimal microarchitecture of 3D-printed β -TCP bone substitutes for vertical bone augmentation differs from that for osteoconduction. *Mater. Des.*, 2021, 204(6): 109650.
10. Zhuang H, Lin R C, Liu Y Q, et al. Three-dimensional-printed bioceramic scaffolds with osteogenic activity for simultaneous photo/magnetothermal therapy of bone tumors. *ACS Biomater. Sci. Eng.*, 2019, 5(12): 6725-6734.
11. Jiang Y L, Yang Y T, Zheng X Y, et al. Multifunctional load-bearing hybrid hydrogel with combined drug release and photothermal conversion functions. *NPG Asia Mater.*, 2020, 12(18): 1-11.
12. Salerno A, Fernandez G M, San Roman B J, et al. Bio-safe fabrication of PLA scaffolds for bone tissue engineering by combining phase separation, porogen leaching and scCO₂ drying. *J. Supercrit. Fluid.*, 2015, 97: 238-246.
13. Wang Y H, Sun L, Mei Z G, et al. 3D printed biodegradable implants as an individualized drug delivery system for local chemotherapy of osteosarcoma. *Mater. Des.*, 2020, 186: 108336.
14. Luo Y X, Li Y X, Qin X L, et al. 3D printing of concentrated alginate/gelatin scaffolds with homogeneous nano apatite coating for bone tissue engineering. *Mater. Des.*, 2018, 146: 12-19.
15. Elias C N, Fernandes D J, Resende C R, et al. Mechanical properties, surface morphology and stability of a modified commercially pure high strength titanium alloy for dental implants. *Dent. Mater.*, 2015, 31(2): 1-13.
16. Sumitomo N, Noritake K, Hattori T, et al. Experiment study on fracture fixation with low rigidity titanium alloy. *J. Mater. Sci.- Mater. M.*, 2008, 19(4): 1581-1586.
17. Xiu P, Jia Z J, Lv J, et al. Tailored surface treatment of 3D printed porous Ti6Al4V by microarc oxidation for enhanced osseointegration via optimized bone in-growth patterns and interlocked bone/implant interface. *ACS Appl. Mater. Interfaces*, 2016, 8: 17964-17975.
18. Nune K C, Li S J, Misra R K. Advancement in three-dimensional titanium alloy mesh scaffolds fabricated by electron beam melting for biomedical devices: mechanical and biological aspects. *Sci. China Mater.*, 2018, 61(4): 455-474.
19. Zhang C Q, Zhang L, Liu L, et al. Mechanical behavior of a titanium alloy scaffold mimicking trabecular structure. *J. Orthop. Surg. Res.*, 2020, 15(1): 40-51.
20. Yin B, Xue B, Wu Z, et al. A novel hybrid 3D-printed titanium scaffold for osteogenesis in a rabbit calvarial defect model. *Am. J. Transl. Res.*, 2018, 10(2): 474-482.
21. Jiang N, Guo Z J, Sun D, et al. Promoting osseointegration of Ti implants through micro/nanoscaled hierarchical Ti phosphate/Ti oxide hybrid coating. *ACS Nano*, 2018, 12: 7883-7891.
22. Liang H, Zhao D L, Feng X B, et al. 3D-printed porous titanium scaffolds incorporating niobium for high bone regeneration capacity. *Mater. Des.*, 2020, 194: 108890.

23. Qiao S C, Sheng Q B, Li Z H, et al. 3D-printed Ti6Al4V scaffolds coated with freeze-dried platelet-rich plasma as bioactive interface for enhancing osseointegration in osteoporosis. *Mater. Des.*, 2020, 194: 108825.
24. Zhang W X, Gu J P, Li K, et al. A hydrogenated black TiO₂ coating with excellent effects for photothermal therapy of bone tumor and bone regeneration. *Mater. Sci. Eng. C*, 2019, 102: 458-470.
25. Yu N, Hu Y, Wang X Y, et al. Dynamically tuning near-infrared-induced photothermal performance of TiO₂ nanocrystals by Nb doping for imaging-guided photothermal therapy of tumors. *Nanoscale*, 2017, 9: 9148-9159.
26. He M M, Zhu C, Xu H, Conducting polyetheretherketone nanocomposites with an electrophoretically deposited bioactive coating for bone tissue regeneration and multimodal therapeutic applications. *ACS Appl. Mater. Interfaces*, 2020, 12: 56924-56934.
27. Guo Z J, Jiang N, Moore J, et al. Nanoscale hybrid coating enables multi-functional tissue scaffold for potential multi-model therapeutic applications. *ACS Appl. Mater. Interfaces*, 2019, 11(30): 27269-27278.
28. Sun D, Mclaughlan J R, Zhang L, et al. Atmospheric pressure plasma synthesized gold nanoparticle/carbon nanotube hybrids for photo-thermal conversion. *Langmuir*, 2019, 35(13): 4577-4588.
29. Lee S Y, Shieh M J. Platinum (II) drug-loaden gold nanoshells for chemo-photothermal therapy in colorectal cancer. *ACS Appl. Mater. Interfaces*, 2020, 12(4): 4254-4264.
30. Su K, Wang C. Recent advances in the use of gelatin in biomedical research. *Biotechnol. Lett.*, 2015, 37: 2139-2145.
31. Sara A, Afra H and Hassan N. Chitosan-gelatin porous scaffold incorporated with chitosan nanoparticles for growth factor delivery in tissue engineering. *Carbohydr. Polym.*, 2018, 15(202): 315-322.
32. Miao X G, Sun D. Graded/gradient porous biomaterials. *Materials*, 2009, 3(1): 26-47.
33. Hur W, Min P, Lee J Y, et al. Bioabsorbable bone plates enabled with local, sustained delivery of alendronate for bone regeneration. *J. Controlled Release*, 2016, 222: 97-106.
34. Yang H, Gao H C and Wang Y J. Hollow hydroxyapatite microsphere: a promising carrier for bone tissue engineering. *J. Microencapsulation*, 2016, 33(5): 421-426.
35. Wang K W, Zhu Y J, Chen F, et al. Microwave-assisted synthesis of hydroxyapatite hollow microspheres in aqueous solution. *Mater. Lett.*, 2011, 65: 2361-2363.
36. Cai B Y, Tan P J, Jiang N, et al. Bioinspired fabrication of calcium-doped TiP coating with nanofibrous microstructure to accelerate osseointegration. *Bioconjugate Chem.*, 2020, 31(6): 1641-1650.
37. Yang H, Hao L J, Zhao N, et al. Hierarchical porous hydroxyapatite microspheres as drug delivery carrier. *CrystEngComm*, 2013, 15: 5760-5763.
38. Donghyun L, Nyoung H D, Jin L S, et al. Suppression of osteoclast formation by gold nanoparticles conjugated alendronate. *Front. Bioeng. Biotechnol.*, 2016, 4: 01825.
39. Lai W, Chen C, Ren X Y, et al. Hydrothermal fabrication of porous hollow hydroxyapatite microspheres for a drug delivery system. *Mater. Sci. Eng. C*, 2016, 62: 166-172.
40. Cai B Y, Jiang N, Tan P J, et al. The custom making of hierarchical micro/nanoscaled titanium phosphate coatings and their formation mechanism analysis. *RSC Adv.*, 2019, 9: 41311-41318.
41. Li Y L, Xiao Y, Liu C S. The horizon of materiobiology: a perspective on material-guided cell

- behaviors and tissue engineering. *Chem. Rev.*, 2017, 117(5): 4376-4421.
42. Zhong Q W, Li W H, Su X P, et al. Degradation pattern of porous CaCO₃ and hydroxyapatite microspheres in vitro and in vivo for potential application in bone tissue. *Colloids Surf. B*, 2016, 143: 56-63.
 43. Zuo Y C, Liu X L, Wei D, et al. Photo-cross-linkable methacrylated gelatin and hydroxyapatite hybrid hydrogel for modularly engineering biomimetic osteon. *ACS Appl. Mater. Interfaces*, 2015, 7: 10386-10394.
 44. Alder R A. Osteoporosis in men: a review. *Bone Res.*, 2014, 2(1): 1-8.
 45. Park J W, Kim Y J, Jiang J H, et al. Effect of phosphoric acid treatment of titanium surfaces on surface properties, osteoblast response and removal of torque forces. *Acta Biomater.*, 2010, 6: 1661-1670.
 46. Gaharwar A K, Mihaila S M, Swami A, et al. Bioactive silicate nanoplatelets for osteogenic differentiation of human mesenchymal stem cells. *Adv. Mater.*, 2013, 25(24): 3329-3336.
 47. Kim M J, Lee B, Yang K, et al. BMP-2 peptide functionalized nanopatterned substrates for enhanced osteogenic differentiation of human mesenchymal stem cells. *Biomaterials*, 2013, 34(30): 7236-7246.
 48. Xu D, Xu L, Zhou C, et al. Salvianolic acid B promotes osteogenesis of human mesenchymal stem cells through activating ERK signaling pathway. *Int. J. Biochem. cell Biol.*, 2014, 51: 1-9.
 49. Zhu X, Eibl O, Scheideler L, et al. Characterization of nano-hydroxyapatite/collagen surfaces and cellular behaviors. *J. Biomed. Mater. Res.*, 2006, 79(1): 114-127.
 50. Frosch S, Nüsse V, Frosch K H, et al. Osseointegration of 3D porous Ti-6Al-4V implants-narrow gap push-out testing and experimental setup considerations. *J. Mech. Behav. Biomed. Mater.*, 2021, 115: 104282.
 51. Fan X P, Feng B, Liu Z Y, et al. Fabrication of TiO₂ nanotubes on porous titanium scaffold and biocompatibility evaluation in vitro and in vivo. *J. Biomed. Mater. Res. A*, 2012, 100A: 3422-3427.